Int. J. Heat Mass Transfer. Vol. 31, No. 8, pp. 1711–1721, 1988
Printed in Great Britain

0017-9310/88 $3.00+0.00

Effect of anisotropic scattering on radiative heat transfer in two-dimensional rectangular enclosures

TAE-KUK KIM and HAEOK LEE
Department of Mechanical Engineering, University of Minnesota, Minneapolis, MN 55455, U.S.A.

(*Received* 19 *November* 1987 *and in final form* 29 *January* 1988)

Abstract—Radiative heat transfer in two-dimensional rectangular enclosures is studied using the *S–N* discrete ordinates method. The medium in the enclosure is gray and absorbs, emits, and anisotropically scatters radiative energy. General Mie-anisotropic phase functions are treated by Legendre polynomial expansions. The average incident radiations and the radiative heat fluxes are presented in graphical and tabular forms. The phase function anisotropy plays a significant role in the radiation heat transfer when the boundary condition is nonsymmetric, but it is not important for symmetric environments. Side wall heat losses are significant for back scattering phase functions, moderate optical thicknesses, large scattering albedos, and small reflectivities.

1. INTRODUCTION

RADIATIVE transfer is an important heat transfer process for high temperature applications such as combustors, nuclear reactors, many industrial processes, and solar energy systems. Radiation has complicated transfer mechanisms that are difficult to model even in a simple system. Early investigations predicted one-dimensional radiative transfer in planar media using various solution techniques. Recent publications in one-dimensional radiative transfer study include general Mie-anisotropic scattering, azimuthal dependence, and non-gray features [1–4]. There has also been considerable effort to solve the multidimensional radiative energy transfer accurately. Two-dimensional isotropic scattering cases are treated by Fiveland [5], using the *S–N* discrete ordinates method, Thynell and Özisik [6], by using the finite element method, and Ratzel and Howell [7], by using the $P-3$ spherical harmonics method. Stephens [8] presents a doubling formulation to be applied to optically thick two-dimensional anisotropic scattering media, and demonstrate it for some isotropic scattering cases. Crosbie and Schrenker [9] also have presented some two-dimensional isotropic scattering results. Three-dimensional $P-3$ results are reported by Mengüc and Viskanta [10]. All the multidimensional cases reported in these references are either for isotropic or simple anisotropic scattering media.

In this study, radiative energy transfer in a two-dimensional rectangular enclosure, with gray, absorbing, emitting, and anisotropically scattering media, is modeled using the *S–N* discrete ordinates method. A complete Mie-scattering phase function is incorporated into the numerical solution. The *S–N* discrete ordinates method, used for this study, is discussed in detail in ref. [11], but a brief outline of the formulations is presented in the following sections. Effects of the anisotropy of the scattering phase functions, the aspect ratio, the optical thickness, the scattering albedo, and the boundary reflectivity, on the radiative transfer are examined. Pure scattering and absorbing–scattering cases are investigated.

A computer code is written for the *S–N* discrete ordinates method in two-dimensional Cartesian coordinates. This program can handle general rectangular enclosure problems, including absorbing, emitting, and anisotropic scattering media with collimated or diffuse incidence. The radiative intensity field, average incident radiation, and the radiative heat flux are obtained using the $S-14$ approximation. The one-dimensional version of the code has been successfully tested against solutions reported in ref. [1], for problems with Mie-scattering phase functions and collimated incidence. Solutions for an isotropically scattering medium in two-dimensional rectangular geometry has also been obtained and compared with published results [5–7]. Two-dimensional Mie-anisotropic scattering cases are presented without comparison, since to our knowledge, there are no published results for these cases.

2. RADIATIVE TRANSFER EQUATION

The radiative transfer equation describing the intensity, I, in a rectangular absorbing, emitting and anisotropically scattering medium is

$$\left[\mu\frac{\partial}{\partial\tau_x}+\xi\frac{\partial}{\partial\tau_y}+1\right]I(\tau_x,\tau_y,\Omega)=S(\tau_x,\tau_y,\Omega) \quad (1)$$

where

$$S(\tau_x,\tau_y,\Omega)=(1-\omega)I_b(\tau_x,\tau_y)+\frac{\omega}{4\pi}\int_{\Omega'}I(\tau_x,\tau_y,\Omega')\Phi(\Omega';\Omega)\,d\Omega' \quad (2)$$

NOMENCLATURE

a	aspect ratio, L/H or τ_{xL}/τ_{yH}
A_e, A_w	control volume face areas normal to the x-coordinate
B_n, B_s	control volume face areas normal to the y-coordinate
C_j	expansion coefficients of phase function
E	emissive power
G	average incident radiation
H	height of the rectangular enclosure
I	monochromatic radiative intensity
l_i	direction cosines: μ if $i=1$; ξ if $i=2$
L	length of the rectangular enclosure
M	total number of ordinate directions
$\mathbf{n}$	inward normal vector to enclosure walls
N	order of phase function expansion
P_j	Legendre polynomials of order j
$\mathbf{Q}$	radiative flux vector
Q_{x_i}	net radiative heat fluxes in the x_i-coordinates
S	source term defined by equation (2)
ΔV	volume of the control volume
w_m	angular weights
w_{xm}	spatial differencing weights of the x-direction
w_{ym}	spatial differencing weights of the y-direction.

Greek symbols

α_m	ratio of spatial mesh size to direction cosine, $\Delta\tau_x/\mu_m$
β	extinction coefficient
γ_m	ratio of spatial mesh size to direction cosine, $\Delta\tau_y/\xi_m$
δ	Dirac delta function
ε_w	wall emissivity
θ	polar angle
κ	absorption coefficient
μ	direction cosine in the x-direction, $\cos\theta$
ξ	direction cosine in the y-direction, $\sin\theta\cos\varphi$
ρ	reflectivity of the enclosure wall
σ_s	scattering coefficient
τ_x, τ_y	optical coordinates, βx and βy, respectively
τ_{xL}, τ_{yH}	overall optical thicknesses, βL and βH, respectively
φ	azimuthal angle
Φ	scattering phase function
ψ	scattering angle
ω	scattering albedo, σ_s/β
Ω	ordinate direction, (μ, ξ).

Superscripts

*	non-dimensional variable
+	positive direction
−	negative direction
′	incident direction.

Subscripts

b	blackbody
m	angular index
n, s, e, w	compass directions
p	control volume center point
w	wall.

and the variables are defined in the Nomenclature. The single scattering phase function may be approximated by a finite series of Legendre polynomials as

$$\Phi(\Omega';\Omega) = \Phi(\cos\psi) = \sum_{j=0}^{N} C_j P_j(\cos\psi) \quad (3)$$

and the argument can be obtained as

$$\cos\psi = \mu\mu' + (1-\mu^2)^{1/2}(1-\mu'^2)^{1/2}\cos(\varphi'-\varphi). \quad (4)$$

The C_j's are the expansion coefficients obtained by the procedure suggested by Clark *et al.* [12]. The required Mie coefficient information is obtained by slightly modifying a code by Wiscombe [13]. The phase function is further expanded by the addition theorem of spherical harmonics [14]. Equation (3) is rewritten using equation (4) as

$$\Phi(\cos\psi) = \Phi(\mu, \varphi; \mu', \varphi') = \sum_{m=0}^{N}(2-\delta_{0,m})\left\{\sum_{j=m}^{N} C_j^m P_j^m(\mu)P_j^m(\mu')\right\} \times \cos m(\varphi'-\varphi) \quad (5)$$

where

$$C_j^m = C_j\frac{(j-m)!}{(j+m)!}$$

and

$$\delta_{0,m} = 1 \text{ if } m = 0$$
$$= 0 \text{ otherwise}$$

and the P_j^m's are the associated Legendre polynomials of order j.

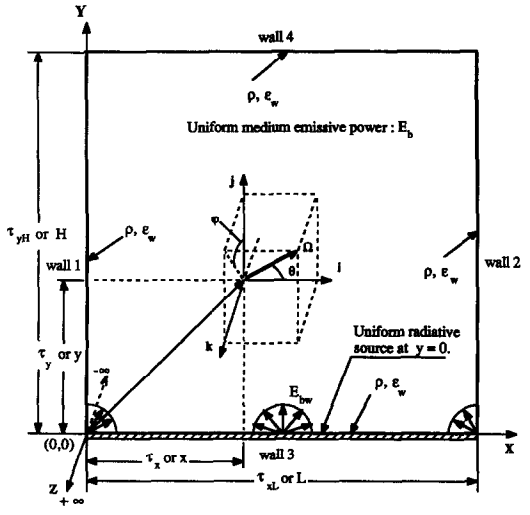

FIG. 1. System geometry.

The radiative transfer equation is to be solved for an enclosure shown in Fig. 1. The rectangular enclosure has an aspect ratio of $a = L/H$. The enclosure walls are gray and diffusely reflecting, and they may also be sources for thermal radiation. The wall intensities are written as

$$I_w(\tau_x, \tau_y, \Omega) = \varepsilon_w I_{bw}(\tau_x, \tau_y) + \frac{\rho}{\pi} \int_{\mathbf{n}\cdot\Omega'<0} |\mathbf{n}\cdot\Omega'| I_w(\tau_x, \tau_y, \Omega')\, d\Omega' \quad \text{for } \mathbf{n}\cdot\Omega > 0. \quad (6)$$

In this study, the diffuse radiative source due to I_{bw} is considered to be nonzero only at the bottom wall (wall 3) for boundary incidence problems.

Once the intensity field is obtained, the average incident radiation and the radiative heat fluxes are obtained as

$$G(\tau_x, \tau_y) = \int_{4\pi} I(\tau_x, \tau_y, \Omega)\, d\Omega \quad (7)$$

$$Q_{x_i}^{+}(\tau_x, \tau_y) = \int_{\mu,\xi>0} l_i I(\tau_x, \tau_y, \Omega)\, d\Omega, \qquad i = 1,2 \quad (8)$$

$$Q_{x_i}^{-}(\tau_x, \tau_y) = \int_{\mu,\xi<0} l_i I(\tau_x, \tau_y, \Omega)\, d\Omega, \qquad i = 1,2 \quad (9)$$

where $i = 1$ indicates the x-direction quantities and $i = 2$ indicates the y-direction quantities. The l_i's are the direction cosines, μ or ξ, for the corresponding coordinates. The net radiative heat fluxes are then obtained by summing up the positive and the negative components of the Q's as

$$Q_{x_i}(\tau_x, \tau_y) = Q_{x_i}^{+}(\tau_x, \tau_y) + Q_{x_i}^{-}(\tau_x, \tau_y) \quad (10)$$

where $Q_{x_i}^{-}$ is always negative by the definition given in equation (9).

3. DISCRETIZATION AND NUMERICAL SOLUTION

The S–N discrete ordinates method replaces the radiative transfer equation with a set of equations for a finite number of M ordinate directions [14]. For a specific ordinate direction m, defined by $\Omega_m = (\mu_m, \xi_m)$, the integral in the source term (equation (2)) is replaced by a quadrature of order M with the appropriate angular weights w_m

$$S(\tau_x, \tau_y, \Omega_m) = (1-\omega) I_b(\tau_x, \tau_y) + \frac{\omega}{4\pi} \sum_{m'=1}^{M} w_{m'} I(\tau_x, \tau_y, \Omega_{m'}) \Phi(\Omega_{m'}; \Omega_m). \quad (11)$$

To solve the discrete ordinates equation, the rectangular enclosure is subdivided into small control volumes by $MX \times MY$ meshes. Within each control volume, the spatially discretized equation for the radiative intensity in the ordinate direction Ω_m is derived as [5]

$$[\mu_m(A_e I_{em} - A_w I_{wm}) + \xi_m(B_n I_{nm} - B_s I_{sm})] + \Delta V I_{pm} = \Delta V S_{pm}, \qquad m = 1, \ldots, M \quad (12)$$

where e, w, n, and s are the boundaries in the compass directions and p is the center point of the control volume. The area and the volume elements are given by considering a unit depth in the z-direction

$$\begin{aligned} A_e &= A_w = \Delta\tau_y \cdot 1 \\ B_n &= B_s = \Delta\tau_x \cdot 1 \\ \Delta V &= \Delta\tau_x \Delta\tau_y \cdot 1 \\ \Delta\tau_x &= (\tau_x)_e - (\tau_x)_w \\ \Delta\tau_y &= (\tau_y)_n - (\tau_y)_s. \end{aligned} \quad (13)$$

The solution of equation (12) approximates the solution of the radiative transfer equation (equation (1)).

The number of unknown I's in equation (12) is reduced by using one of several relationships between the control volume boundary intensities and the center point intensity [11]. The weighted diamond difference scheme is used in this study to relate the intensities in the control volume. The weighted relationship of the cell boundary intensities to the average intensity in the cell is expressed as

$$\begin{aligned} I_{pm} &= w_{xm} I_{em} + (1 - w_{xm}) I_{wm} \\ &= w_{ym} I_{nm} + (1 - w_{ym}) I_{sm} \end{aligned} \quad (14)$$

when both of the direction cosines, μ_m and ξ_m, are positive. If μ_m is negative, I_{em} is multiplied by $(1 - w_{xm})$ and I_{wm} by w_{xm}. The y-direction relationship also obeys a similar rule. The w_{xm} and w_{ym} are appropriate differencing weights in the x- and the y-directions, taken between 0.5 and 1. For example, $w_{xm} = w_{ym} = 1$ denotes a step function relation, which gives less accurate results, and $w_{xm} = w_{ym} = 0.5$ denotes the standard diamond difference. When the weights are equal to 0.5, this sometimes results in unrealistic negative intensities during the solution process. To avoid

this abnormal situation, a positive scheme suggested by Lathrop [15] is applied in selecting the differencing weights. For the positive μ_m and ξ_m, the expressions for the differencing weights are

$$w_{xm} = 1 - \frac{\gamma_m}{\alpha_m(\gamma_m + 2)} \quad \text{with} \quad w_{xm} = \max(w_{xm}, 0.5) \tag{15a}$$

$$w_{ym} = 1 - \frac{\alpha_m}{\gamma_m(\alpha_m + 2)} \quad \text{with} \quad w_{ym} = \max(w_{ym}, 0.5) \tag{15b}$$

where $\alpha_m = \Delta\tau_x/\mu_m$ and $\gamma_m = \Delta\tau_y/\xi_m$.

If I_{wm} and I_{sm} are assumed to be known, where the iteration is in a direction of positive direction cosines and in the increasing space dimensions, then the equation (12) can be reduced to eliminate the intensities I_{em} and I_{nm}, using equation (14). Solving for I_{pm} yields

$$I_{pm} = \frac{\mu_m A I_{wm} + \xi_m B I_{sm} + \Delta V S_{pm}}{\mu_m A_e/w_{xm} + \xi_m B_n/w_{ym} + \Delta V} \quad \text{for} \quad \mu_m, \xi_m > 0 \tag{16}$$

where

$$A = (1 - w_{xm})A_e/w_{xm} + A_w$$

$$B = (1 - w_{ym})B_n/w_{ym} + B_s.$$

The boundary condition expressed in equation (6) can also be expressed in a discretized form for each boundary wall. These expressions are similar to those found in ref. [5]. Equations (11) and (16) are used to construct a numerical code, which solves for the angular intensity distribution at every grid point in the medium. The required ordinates set, μ_m and ξ_m, and the corresponding angular weights, w_m, are taken from the code TWOTRAN [16].

An iterative solution of equation (16) is required, since the source terms, S_{pm}, are functions of the unknown cell average intensities, I_{pm}. The source terms for equation (16) are computed from the intensity values of the previous iterations, by using equation (11). After the new intensity values are obtained, the source terms are recomputed using the updated cell average intensities. The initial values for the I_{pm}'s are set equal to zero, i.e. the source terms are all zero in the beginning of the solution. For fast iteration convergence, and to avoid unnecessary coupling between the discrete ordinate equations, a special spatial–angular iteration procedure [16] is applied to the solution.

As a means to check the energy balance in each control volume, and to accelerate the convergence of the numerical solution, the energy balance is computed during every iteration. This is done by considering the total gain and the total loss from a control volume. Rebalance factors are introduced to assure a correct balance of the energy in each control volume, and the corresponding intensities are multiplied by these factors. When the energy is balanced in a control volume, the rebalance factor for that control volume should be equal to one.

To derive the expressions for the rebalance factors, an expression for the divergence of the radiative flux [17] is used, which is of the form

$$\nabla \cdot \mathbf{Q} = 4\pi(1-\omega)\left[I_b(\tau_x, \tau_y) - \frac{1}{4\pi}\int_{\Omega'} I(\tau_x, \tau_y, \Omega')\, d\Omega' \right]. \tag{17}$$

If any of the rebalance factors have negative values or do not converge after a given iteration limit, a representative rebalance factor for the whole system is obtained by balancing the overall energy of the system. A detailed discussion of the rebalance technique can be found in ref. [16].

Convergence is checked during the iteration process using the cell average intensities at the current and the previous iterations. It is assumed that the convergence is obtained, when the maximum percentage error of the intensities is less than 0.0001%.

4. RESULTS

A discussion of the numerical study performed for some selected cases is given below. Since this study focuses on the effect of anisotropic scattering, most of the cases considered are pure scattering ($\omega = 1$), where the scattering is most significant. The phase functions listed in Table 1 and also shown in Fig. 2, are studied to examine the effect of anisotropy. The expansion coefficients for the phase functions F1 and F2 are computed from the modified Mie code with the particle size parameters of 5 and 2, respectively, for a refractive index of (1.33, 0). Coefficients for B1 are cited from Özisik [18], for a size parameter of 1 and an infinite refractive index. B2 is obtained from a phase function expression for small particles with very large refractive indices [17]. The asymmetry factors of the phase functions are also given in Table 1 as $C_1/3$ [19].

For the numerical study, the enclosure is subdivided into 26×26 control volumes, for all the cases except for optical thicknesses larger than 2.5, where 52×52 control volumes are used. Due to the enormous amounts of computer time, finer mesh solutions are not attempted (40–120 CPU s for 26×26 cases, and 800–1700 CPU s for 52×52 cases on Cray 2).

The $S-14$ approximation, which computes 112 fluxes over the hemisphere, is used for all of the cases considered. For the phase functions considered in this study, the $S-14$ approximation is quite accurate. Several different orders of S–N solutions are compared in Fig. 3, which shows the net radiative heat flux, Q_y^*, along the centerline, for a boundary incidence problem. The phase function F2 is considered to demonstrate the convergence of the solution. The heat flux results are shown to not change noticeably above the $S-10$ approximation, and the $S-14$ results are shown to be quite accurate. If $S-16$ is taken as

Table 1. C_j, the expansion coefficients for the phase functions

j	F1	F2	B1	B2
0	1.00000	1.00000	1.00000	1.00000
1	2.53602	2.00917	−0.56524	−1.20000
2	3.56549	1.56339	0.29783	0.50000
3	3.97976	0.67407	0.08571	
4	4.00292	0.22215	0.01003	
5	3.66401	0.04725	0.00063	
6	3.01601	0.00671		
7	2.23304	0.00068		
8	1.30251	0.00005		
9	0.53463			
10	0.20136			
11	0.05480			
12	0.01099			
Number of terms	13	9	6	3
$C_1/3$	0.84534	0.66972	−0.18841	−0.40000
Average percentage error				
$S-14$	1.76454	0.07127	0.00321	0.000009

Note: F indicates that the phase function has peak values in the forward direction and B in the backward direction.

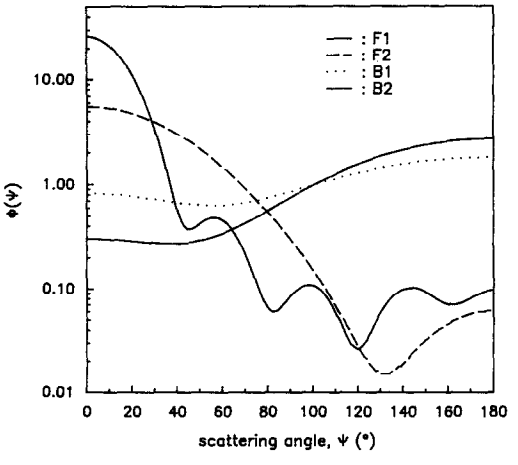

FIG. 2. Scattering phase functions.

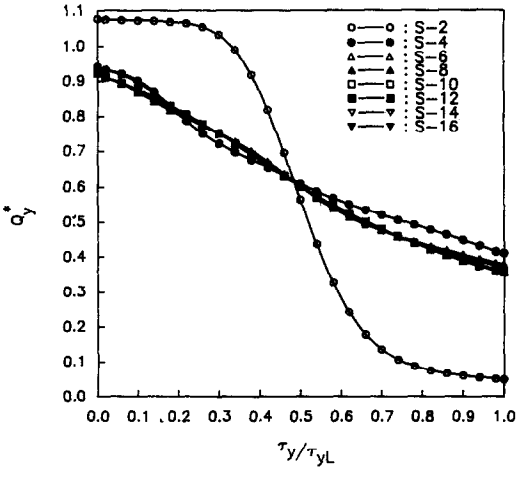

FIG. 3. Comparison of the different orders of S–N approximation for F2 phase function ($\rho = 0$, $\omega = 1.0$, $\tau_{xL} = \tau_{yL} = 1.0$).

the exact solution, the $S-14$ approximation for F2 results in 0.0556% average error and the F1 results in 0.1036% average error.

A further indication of the $S-14$ accuracy is shown by checking the normalization of the phase functions. The inaccuracy of anisotropic scattering solutions is mainly due to the error in the integration of the phase function. The normalization of the phase function is described by

$$\frac{1}{4\pi}\int_{4\pi}\Phi(\Omega';\Omega)\,d\Omega' = 1. \tag{18}$$

The percentage error of the phase function normalization for direction m is then obtained as

$$(\%\ \text{error})_m = \left|1-\frac{1}{4\pi}\sum_{m'=1}^{M} w_{m'}\Phi_{m'm}\right|\times 100. \tag{19}$$

As shown in Table 1, all the phase functions considered normalize to less than 0.1% average error except for F1, when the $S-14$ approximation is used. The average normalization error of F1 for $S-16$ is 1.4576%, showing only a slight improvement over the $S-14$ result. For highly anisotropic phase functions, a higher order S–N approximation should give better results. The improvement for the F1 phase function using the $S-16$ approximation is found to be small.

Using the $S-14$ approximation, enormous amounts of data have been generated, including the radiative intensity, the average incident radiation, and the heat flux over the whole region in the enclosure. Presentation is limited only to the quantities of average incident radiation and radiative heat flux,

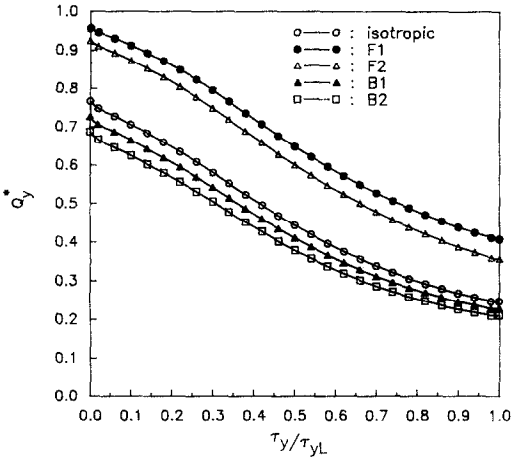

FIG. 4. Effect of anisotropy on the centerline net radiative heat flux in the y-direction ($\rho = 0$, $\omega = 1.0$, and $\tau_{xL} = \tau_{yL} = 1.0$).

which are important to heat transfer. Intensity data are not provided in this paper. Dimensionless quantities, $G^* = G/4E$, $Q_y^* = Q_y/E$, $Q_y^{+*} = Q_y^+/E$, and $Q_y^{-*} = Q_y^-/E$, where E represents E_{bw} for boundary incidence problems and E_b for isothermal emission problems, are presented.

4.1. *Boundary incidence problems*

Boundary incidence problems are studied, where one wall is kept hot, but all other walls and the medium are kept cold. $E_{bw3} = E_{bw} = \text{const.}$ and $E_{bwi} = E_b = 0$ for $i = 1$, 2 and 4, i.e. the radiative energy source is applied only at $\tau_y = 0$. The effect of the anisotropy on the radiative heat transfer is most significant for non-symmetric environments, and the boundary incidence problems are good examples for studying this effect. Effects of other important parameters on the radiative heat transfer are also examined. These parameters are the aspect ratio of the enclosure, the scattering albedo, the wall reflectivity, and the optical thickness.

The net radiative heat fluxes in the y-direction, Q_y^*'s, along the centerline ($\tau_x = 0.5\tau_{xL}$) of a black square enclosure are presented in Fig. 4, for pure scattering media with different phase functions. In Table 2, the corresponding data set is provided for reference. Forward scattering media transfer more radiative heat than the isotropic scattering media, while the backward scattering media transport less radiative heat through the media than the isotropic media. The amount of enhancement or reduction in the energy transport is also seen to be related to the degree of anisotropy associated with each phase function (Table 1). The transmitted Q_y^{+*} computed at the far wall, away from the hot wall source ($\tau_y = \tau_{yH}$), also indicates the same effect of anisotropy that is shown with the net radiative heat flux. The forward scattering phase functions also reduce the side wall heat losses.

The effect of the aspect ratio on the radiative heat transfer are examined in Fig. 5 for pure scattering media, using phase function F2. Corresponding one-dimensional $S-14$ results are also presented as a limiting solution. Figure 5 shows the centerline net radiative heat fluxes in the y-direction, with the aspect ratio as the parameter. One-dimensional net radiative heat flux for pure scattering is a constant over the whole slab thickness since $\nabla \cdot \mathbf{Q} = 0$, and in this case, $(Q_y^*)_{1\text{-}D} = 0.7662$. Two-dimensional Q_y^* deviates greatly from the one-dimensional result when $a = 1$. As the aspect ratio is increased, Q_y^* becomes flatter and approaches the one-dimensional result. For $a = 10$, Q_y^* is a nearly constant average value of 0.7635, which is very close to the one-dimensional result. For other phase functions listed in Table 1, similar trends are observed for the varying aspect ratios. The different magnitudes for Q_y^*, which can result due to the different anisotropies of the phase functions, can be seen from the $a = 1$ result in Fig. 4.

Figure 6 shows the net radiative heat fluxes along the centerline of scattering media (phase function F2) with different scattering albedos. The slope of the Q_y^* distribution along the centerline is steepest when $\omega = 0$, since energy absorption by the medium reduces the radiative heat transfer. As ω is increased, the absorption becomes less important while the scattering becomes dominant, causing larger side wall heat losses and appreciable but small Q_y^{-*} components. Therefore, Q_y^* becomes larger as ω is increased except near the hot wall where the back scattered Q_y^{-*} is large for large ω.

The wall reflectivity, ρ, also plays a significant role in the radiative heat transfer. Figure 7 shows the net radiative heat fluxes along the centerline of the enclosure. The data shown are for a gray square enclosure of unit optical thickness, containing a pure scattering medium (phase function F2). Q_y^* is affected significantly by the different ρ's, because the boundary emission source term in equation (6) is proportional to $\varepsilon_w = 1 - \rho$. For small ρ's, the boundary emission source term is large, while the radiative fluxes reflected back from the other walls are small. This causes a large radiative energy loss through the cold walls. As ρ is increased, the emission source term becomes small. The angular distribution of the radiative intensity also becomes more uniform, and Q_y^* decreases with increasing ρ. When $\rho = 0.9$, Q_y^* is quite small, and the angular distribution of the radiative intensity is nearly uniform at all the locations in the medium. The heat flux is reduced by a factor of 10, when ρ is changed from 0 to 0.9 at $\tau_y = 0$ due to a small emission source. For a limiting case of $\rho = 1$, the boundary emission source term in equation (6) becomes zero since ε_w is zero, and Q_y^* is zero everywhere. Therefore, the radiation has no contribution to the heat transfer. The side wall heat losses are largest for $\rho = 0$.

The optical thickness is another important parameter for radiative heat transfer. Cases with different optical thicknesses are studied for a pure scattering medium (phase function F2). In Fig. 8, the centerline

Table 2. Q_y^*'s along the centerline ($\tau_x/\tau_{xL} = 0.5$) for different phase functions: $\rho = 0$, $\omega = 1.0$, $\tau_{xL} = \tau_{yL} = 1.0$

τ_y/τ_{yL}	ISO	F1	F2	B1	B2
0.000	0.766958	0.956813	0.923827	0.726575	0.687178
0.020	0.747546	0.945954	0.909987	0.706159	0.665768
0.060	0.728379	0.930752	0.893455	0.686828	0.646392
0.100	0.706271	0.911806	0.873262	0.664805	0.624567
0.140	0.683518	0.892072	0.851966	0.642318	0.602443
0.180	0.660155	0.871542	0.829618	0.619373	0.579992
0.220	0.635295	0.848916	0.805209	0.595081	0.556332
0.260	0.608619	0.823535	0.778325	0.569125	0.531152
0.300	0.580580	0.795751	0.749412	0.541947	0.504883
0.340	0.551957	0.766425	0.719313	0.514303	0.478258
0.380	0.523486	0.736463	0.688861	0.486905	0.451960
0.420	0.495735	0.706615	0.658723	0.460295	0.426506
0.460	0.469084	0.677425	0.629366	0.434831	0.402230
0.500	0.443748	0.649236	0.601073	0.410712	0.379316
0.540	0.419826	0.622244	0.573995	0.388026	0.357839
0.580	0.397358	0.596557	0.548208	0.366802	0.337817
0.620	0.376352	0.572229	0.523748	0.347042	0.319247
0.660	0.356797	0.549284	0.500628	0.328729	0.302108
0.700	0.338667	0.527717	0.478836	0.311831	0.286362
0.740	0.321920	0.507498	0.458344	0.296300	0.271957
0.780	0.306497	0.488580	0.439109	0.282073	0.258824
0.820	0.292332	0.470905	0.421082	0.269074	0.246886
0.860	0.279361	0.454411	0.404216	0.257232	0.236062
0.900	0.267533	0.439043	0.388476	0.246487	0.226286
0.940	0.256818	0.424754	0.373843	0.236797	0.217509
0.980	0.247184	0.411503	0.360318	0.228112	0.209670
1.000	0.247123	0.407981	0.357322	0.228617	0.210689

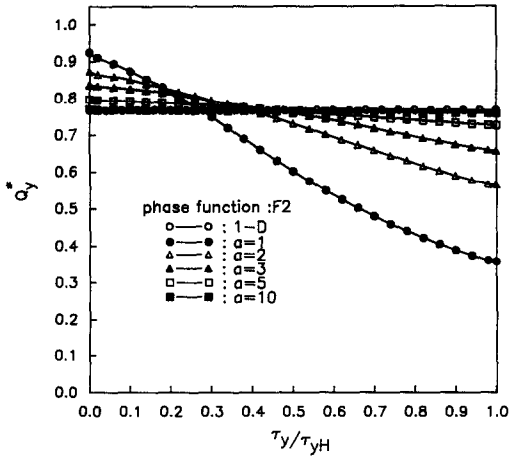

FIG. 5. Effect of the aspect ratio on the centerline net radiative heat flux in the y-direction (1-D vs 2-D) ($\rho = 0$, $\omega = 1.0$, and $\tau_{xL} = \tau_{yL} = 1.0$).

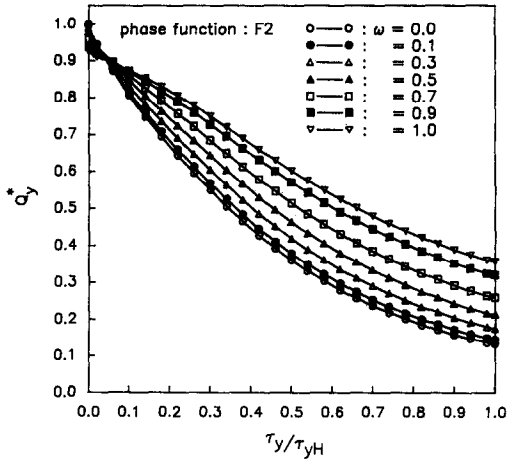

FIG. 6. Effect of the scattering albedo on the centerline net radiative heat flux in the y-direction ($\rho = 0$ and $\tau_{xL} = \tau_{yL} = 1.0$).

net radiative heat fluxes in the y-direction are presented with the optical thickness as the parameter. Q_y^*'s are large at small optical thicknesses since the resistance through the medium is small ($Q_y^-{}^*$ is much smaller compared to $Q_y^+{}^*$), and they decrease to small values and become flatter at large optical thicknesses due to larger heat resistances. For a large optical thickness of 10, centerline Q_y^* varies from 0.51072 at $\tau_y = 0$ to 0.11005 at $\tau_y = \tau_{yL}$. This distribution is quite different from the 1-D uniform result of 0.28462, due to the side wall heat loss for the square enclosure. When the optical thickness becomes very large, the trends shown in Fig. 8 suggest that the two-dimensional result should approach the uniform one-dimensional result of nearly zero flux at the centerline. Figure 8 also shows the numerical error associated with a finite grid near the hot wall. Using a finer grid of 52×52 control volumes eliminates the error for $\tau = 2.5$. Finer or non-uniform grids would improve the results for larger optical depths.

The distribution of Q_y^*, evaluated at different x positions along the hot surface ($\tau_y = 0$), provides another view of the effect of the various parameters on the radiative transfer. In Fig. 9, the hot wall Q_y^*

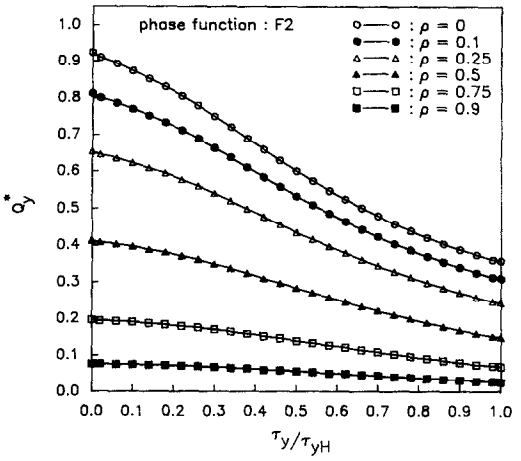

FIG. 7. Effect of wall reflectivity on the centerline net radiative heat flux in the y-direction ($\omega = 1.0$ and $\tau_{xL} = \tau_{yL} = 1.0$).

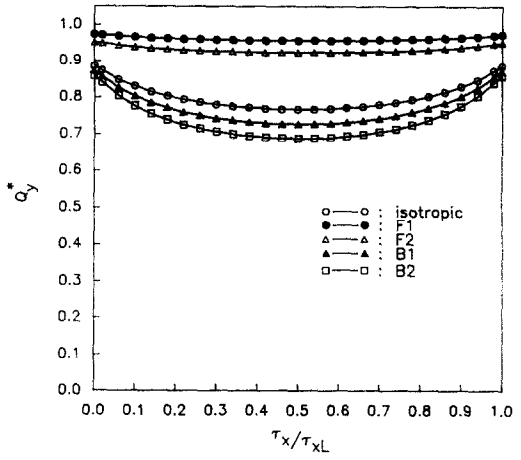

FIG. 9. Effect of anisotropy on the net hot surface radiative heat flux ($\rho = 0$, $\omega = 1.0$, and $\tau_{xL} = \tau_{yL} = 1.0$).

distribution is shown for different scattering phase functions. In comparison to the isotropic scattering, the forward scattering phase functions tend to enhance the radiative heat release from the hot wall, and the backward scattering phase functions tend to reduce it. The amount of heat release is then related to the degree and the sign of the phase function anisotropy.

The hot wall Q_y^* distribution along the x-direction has also been examined for the effect of other parameters also, although the data are not presented here. The hot wall Q_y^* is 1 at $\omega = 0$, since there is no backscattered radiation ($Q_y^-{}^* = 0$ but $Q_y^+{}^* = 1$ at the hot wall when $\rho = 0$). It decreases monotonically with an increasing ω, since the backscattered radiation increases with increasing ω. Optical thickness effects also show a similar trend as for ω. At small optical thickness, Q_y^* has nearly a uniform value of 1.0 (similar to the optically thin plane parallel solution), since the medium reflects back negligible amounts of energy, while the energy transferred away from the hot wall remains unchanged. As the optical thickness is increased, the heat transfer rates are decreased. Heat released from the hot wall in the two-dimensional problem is much larger than in the one-dimensional case for the same optical thickness. This is because the two-dimensional medium loses large amounts of energy through the side walls, and therefore requires a larger energy supplied to the hot wall to maintain the constant temperature.

The average incident radiation, G^*'s, which indicate the average level of the radiation intensity, are shown in Fig. 10 (data set in Table 3) for various scattering phase functions. For different scattering phase functions, the G^*'s vary most significantly for the $\omega = 1$ case when $\rho = 0$. As compared to the isotropic results, flatter distributions of G^* are observed for the forward scattering phase functions, since the radiative intensity scattered away from the centerline is small and the transmitted intensity is large. The G^*'s for the backward scattering phase functions show steeper distributions than isotropic, since the

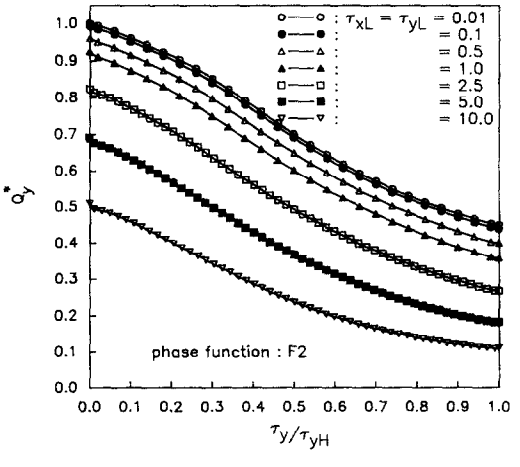

FIG. 8. Effect of the optical thickness on the centerline net radiative heat flux in the y-direction ($\rho = 0$ and $\omega = 1.0$).

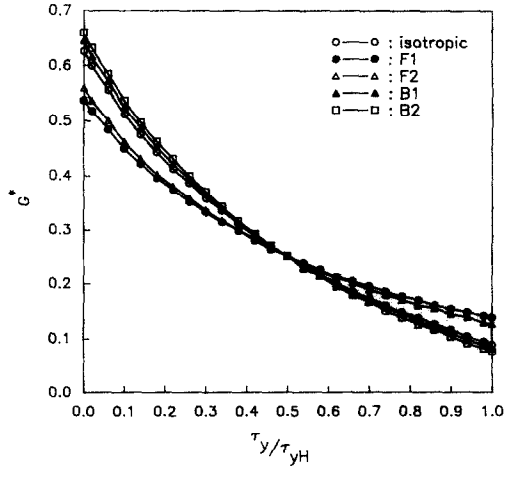

FIG. 10. Effect of anisotropy on the centerline average incident radiation ($\rho = 0$, $\omega = 1.0$, and $\tau_{xL} = \tau_{yL} = 1.0$).

Table 3. G^*'s along the centerline ($\tau_x/\tau_{xL} = 0.5$) for different phase functions: $\rho = 0$, $\omega = 1.0$, $\tau_{xL} = \tau_{yL} = 1.0$

τ_y/τ_{yL}	ISO	F1	F2	B1	B2
0.000	0.626625	0.537238	0.557988	0.643562	0.660444
0.020	0.600355	0.518740	0.535868	0.616569	0.632666
0.060	0.556250	0.484921	0.498624	0.570840	0.585263
0.100	0.512708	0.449798	0.461528	0.525645	0.538400
0.140	0.474531	0.419550	0.429650	0.485822	0.496928
0.180	0.441868	0.394810	0.403170	0.451563	0.461070
0.220	0.412683	0.373385	0.379963	0.420857	0.428843
0.260	0.385379	0.353413	0.358333	0.392118	0.398681
0.300	0.359364	0.334146	0.337640	0.364761	0.369998
0.340	0.334617	0.315545	0.317857	0.338761	0.342773
0.380	0.311256	0.297782	0.299127	0.314241	0.317122
0.420	0.289369	0.281022	0.281556	0.291279	0.293117
0.460	0.268964	0.265367	0.265191	0.269885	0.270764
0.500	0.249999	0.250859	0.250021	0.250002	0.249999
0.540	0.232387	0.237473	0.235981	0.231539	0.230725
0.580	0.216013	0.225155	0.222990	0.214376	0.212815
0.620	0.200763	0.213820	0.210952	0.198395	0.196136
0.660	0.186516	0.203371	0.199764	0.183463	0.180560
0.700	0.173155	0.193714	0.189331	0.169461	0.165955
0.740	0.160570	0.184751	0.179558	0.156275	0.152204
0.780	0.148657	0.176397	0.170359	0.143791	0.139191
0.820	0.137300	0.168568	0.161635	0.131900	0.126801
0.860	0.126371	0.161186	0.153281	0.120471	0.114907
0.900	0.115699	0.154161	0.145179	0.109337	0.103343
0.940	0.105067	0.147404	0.137162	0.098291	0.091917
0.980	0.094238	0.140816	0.129025	0.087135	0.080447
1.000	0.088360	0.138057	0.125029	0.081141	0.074333

radiative intensity scattered away from the centerline is large and the transmitted intensity is small due to the large backscattered component.

When $\omega = 0$, G^* is small, since most of the radiative energy is absorbed by the cold medium, while the medium emits and scatters no radiative energy. As ω is increased from 0 to 1, G^* increases, since the absorption is reduced relative to scattering. At $\omega = 1$, the largest average intensity distribution is obtained. For small albedos, the variations due to different scattering phase functions are then small compared to the $\omega = 1$ results. For isotropic media in gray enclosures, refs. [5, 7] report a similar effect due to different ρ's as was found in this anisotropic media study. However, the magnitudes and the slopes of G^*'s are strongly dependent upon the scattering phase functions used.

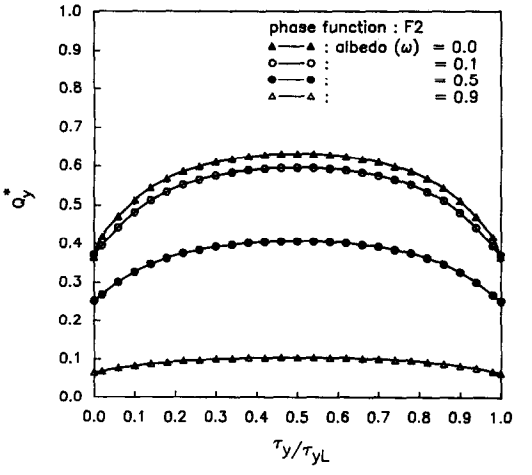

FIG. 11. Net radiative heat flux at the wall for isothermally emitting media ($\rho = 0$ and $\tau_{xL} = \tau_{yL} = 1.0$).

4.2. *Isothermal emission problems*

Another simple problem considered in this study is the isothermal emission case, where all the boundary sources are zero, and the medium in the black square enclosure emits uniform radiative energy over the whole region. That is, $E_{bw1} = E_{bw2} = E_{bw3} = E_{bw4} = 0$ and E_b = constant.

The effect of anisotropy on isothermal emission is found not to be important when symmetric boundary conditions are considered. The anisotropic effects cancel out, and the resulting intensity field looks like that of isotropic scattering. The average incident radiation and the radiative heat flux obtained for different anisotropic phase functions are very similar to each other in their magnitudes and distributions. This same conclusion holds true for both the one- and two-dimensional geometries that have been tested. Since the results obtained with different phase functions are all similar, only the isothermal emission result obtained for the phase function F2 is presented in Fig. 11.

Figure 11 shows the net radiative heat transfer rates at a boundary surface for different albedos. Solution of the isothermal emission problems with no other radiative source is strongly dependent upon the scat-

tering albedo. When ω is close to one, the radiative source, equation (2), is nearly zero. For pure scattering there is no source. As ω becomes close to zero, the source becomes large, and the largest source contribution is obtained for the non-scattering case of $\omega = 0$.

5. CONCLUSIONS

Numerical solutions of the radiative heat transfer in rectangular enclosures, with general Mie-anisotropic scattering media, has been obtained using the accurate *S–N* discrete ordinates method. Benchmark radiative heat transfer results are provided for anisotropic scattering media described by four different phase functions. The heat transfer quantities of heat flux and average incident radiation are obtained from the radiative intensity solutions. The $S-14$ results presented in this paper are quite accurate and will serve as a reference for later studies on radiative heat transfer in similar geometries. A parametric study reveals strong effects of the anisotropy on the radiative heat transfer in absorbing–scattering media, when the environment is nonsymmetric. For a symmetric environment, the anisotropic effects are cancelled out to give an isotropic result, regardless of the anisotropy of the phase functions applied.

Acknowledgements—This work was supported in part by the National Science Foundation Grant No. NSF/CBT-8451076. The PYI award was partly supported by the Exxon Corporation. A grant from the Minnesota Supercomputer Institute is also gratefully acknowledged.

REFERENCES

1. R. D. M. Garcia and C. E. Siewert, Benchmark results in radiative transfer, *Transp. Theory Statist. Phys.* **14**(4), 437–483 (1985).
2. H. Lee and R. O. Buckius, Scaling anisotropic scattering in radiation heat transfer for a planar medium, *Trans. ASME* **104,** 68–75 (1982).
3. M. F. Modest and F. H. Azad, The influence and treatment of Mie-anisotropic scattering in radiative heat transfer, *Trans. ASME* **102,** 92–98 (1980).
4. C. Flicke, The phase-integral method for radiative transfer problems with highly-peaked phase functions, *J. Quant. Spectrosc. Radiat. Transfer* **20,** 429–445 (1978).
5. W. A. Fiveland, Discrete-ordinates solutions of the radiative transport equation for rectangular enclosures, *J. Heat Transfer* **106,** 699–706 (1984).
6. S. T. Thynell and M. N. Özisik, Radiation transfer in isotropically scattering rectangular enclosures, *J. Thermophys.* **1**(1), 69–76 (1987).
7. A. C. Ratzel III and J. R. Howell, Two-dimensional radiation in absorbing–emitting–scattering media using the *P–N* approximation, ASME Paper, 82-HT-19 (1982).
8. G. L. Stephens, Radiative transfer in spatially heterogeneous, two-dimensional, anisotropically scattering media, *J. Quant. Spectrosc. Radiat. Transfer* **36**(1), 51–67 (1986).
9. A. L. Crosbie and R. G. Schrenker, Multiple scattering in a two-dimensional rectangular medium exposed to collimated radiation, *J. Quant. Spectrosc. Radiat. Transfer* **33**(2), 101–125 (1985).
10. M. P. Mengüc and R. Viskanta, Radiative transfer in three-dimensional rectangular enclosures containing inhomogeneous, anisotropically scattering media, *J. Quant. Spectrosc. Radiat. Transfer* **33**(6), 533–549 (1985).
11. B. G. Carlson and K. D. Lathrop, Transport theory—the method of discrete-ordinates. In *Computing Methods in Reactor Physics* (Edited by H. Greenspan, C. N. Kelber and D. Okrent). Gordon & Breach, New York (1968).
12. G. C. Clark, C. M. Chu and S. W. Churchill, Angular distribution coefficients for radiation scattered by a spherical particle, *J. Opt. Soc. Am.* **47**(1), 81–84 (1957).
13. W. J. Wiscombe, Improved Mie scattering algorithms, *Appl. Optics* **19**(9), 1505–1509 (1980).
14. S. Chandrasekhar, *Radiative Transfer*, pp. 149–150. Dover, New York (1960).
15. K. D. Lathrop, Spatial differencing of the transport equation: positivity vs accuracy, *J. Computational Phys.* **4,** 475–498 (1968).
16. K. D. Lathrop and F. W. Brinkley, TWOTRAN-II: an interfaced, exportable version of the TWOTRAN code for two-dimensional transport, Los Alamos Scientific Laboratory Report #LA-4848-MS (1973).
17. R. Siegel and J. R. Howell, *Thermal Radiation Heat Transfer*, 2nd Edn, pp. 461–462 and 591. McGraw-Hill, New York (1981).
18. M. N. Özisik, *Radiative Transfer*, p. 83. Wiley-Interscience, New York (1973).
19. W. M. Irvine, The asymmetry of the scattering diagram of a spherical particle, *Bull. Astr. Insts Neth.* **17**(3), 176–184 (1963).

EFFET DE LA DIFFUSION ANISOTROPE SUR LE TRANSFERT RADIATIF DANS DES CAVITES RECTANGULAIRES BIDIMENSIONNELLES

Résumé—Le transfert de chaleur radiatif dans des cavités rectangulaires bidimensionnelles est étudié en utilisant la méthode des ordonnées discrètes *S–N*. Le milieu dans la cavité est gris et il absorbe, émet et diffuse de façon anisotrope l'énergie radiante. Les fonctions de phases anisotropes de Mie sont traitées par des développements en polynômes de Legendre. Les rayonnements incidents moyens et les flux de chaleur radiatifs sont présentés sous forme de graphiques et de tables. L'anisotropie des fonctions de phase joue un rôle sensible dans le transfert de chaleur par rayonnement quand la condition limite n'est pas symétrique, mais peu important pour des environnements symétriques. Les pertes de chaleur par les parois latérales sont significatives pour des fonctions de phase de rétrodiffusion, des épaisseurs optiques modérées, des albedos importants, et des faibles réflectivités de surface.

EINFLUSS EINER ANISOTROPEN STREUUNG BEI DER WÄRMEÜBERTRAGUNG DURCH STRAHLUNG IN ZWEIDIMENSIONALEN RECHTWINKLIGEN HOHLRÄUMEN

Zusammenfassung—Der Wärmetransport durch Strahlung in zweidimensionalen rechtwinkligen Hohlräumen wurde unter Verwendung der *S–N*-Methode mit diskreten Ordinaten untersucht. Das Medium im Hohlraum ist grau und absorbiert, emittiert und streut anisotrop Strahlungsenergie. Allgemeine Mie-anisotrope Phasenfunktionen werden mit Legendre'schen Polynomausdrücken dargestellt. Die mittlere eingefallene Strahlung und der Wärme fluß durch Strahlung sind in grafischer und tabellarischer Form dargestellt. Die Anisotropie der Phasenfunktionen spielt eine entscheidende Rolle beim Wärmetransport durch Strahlung, wenn die Randbedingungen nicht-symmetrisch sind ; sie ist jedoch bei einer symmetrischen Umbegung unwichtig. Die Wärmeverluste durch die Seitenwände sind signifikant für Phasenfunktionen bei Rückstrahlung, mäßige optische Dicken, große Streuungsalbedos und geringe Oberflächenreflektivitäten.

ВЛИЯНИЕ АНИЗОТРОПНОГО РАССЕЯНИЯ НА ЛУЧИСТЫЙ ТЕПЛОПЕРЕНОС В ДВУМЕРНЫХ ПРЯМОУГОЛЬНЫХ ПОЛОСТЯХ

Аннотация—Методом дискретных ординат *S–N* исследуется лучистый теплоперенос в двумерных прямоугольных полостях. Среда в полости является серой, поглощающей, излучающей и анизотропно рассеивающей. Общие анизотропные фазовые функции Ми рассматриваются с помощью разложений в ряд полиномов Лежандра. Средние значения падающего излучения и лучистые тепловые потоки представлены графически и в виде таблиц. Анизотропия фазовой функции играет важную роль при лучистом теплопереносе, когда граничное условие является несимметричным, но несущественна в симметричном окружении. Потери тепла боковыми стенками значительны для фазовых функций рассеяния назад, для средних оптических толщин, больших значений альбедо рассеяния и малого отражения от поверхности.